Nanoscale Advances

ROYAL SOCIETY OF CHEMISTRY

PAPER

View Article Online
View Journal | View Issue

Cite this: *Nanoscale Adv.*, 2025, **7**, 6179

Unlocking exceptional EMI shielding in $Ti_3C_2T_x$ MXenes through controlled microstructure and surface chemistry

Shahzad Hussain, *[a] Resham Siddique,[a] Muhammad Nadeem,[b] Eman Zafar,[a] Sadia Manzoor[a] and Jawwad A. Darr[c]

The rapid advancement of highly integrated electronics demands next-generation electromagnetic interference (EMI) shielding materials that combine lightweight, ultrathin, flexible, and mechanically robust properties with exceptional shielding effectiveness (SE) to mitigate signal crosstalk and ensure device reliability. In this work, we demonstrate the fabrication of high-performance EMI shields using highly conductive, additive-free aqueous $Ti_3C_2T_x$ (T = O, OH, Cl, F) MXene dispersions synthesized under both harsh and mild etching conditions. These dispersions were engineered into freestanding thin films and functionalized cotton fabrics *via* vacuum-assisted filtration, enabling tunable EMI shielding properties through precise control of etchant chemistry, flake size, microstructure, thickness, and MXene loading. The EMI shielding improved with film thickness, and the 13 μm thick film demonstrated exceptional EMI shielding of 60 dB. The freestanding heat-treated $Ti_3C_2T_x$ film with a minimal thickness of 5 μm achieved a remarkable shielding effectiveness of 71 dB (which is 37% higher than that of the untreated film) corresponding to 99.99999% EMI attenuation. This film also exhibited an ultrahigh absolute shielding effectiveness (SSE_T) of 72 300 dB cm^2 g^{-1}, surpassing all previously reported MXene-based shields of comparable thickness. The improved stability was attributed to the thermal conversion of surface OH groups to O-terminations, reducing interflake spacing and enhancing conductivity. The coated cotton fabric achieved an unprecedented SE of 82 dB due to the excellent wave attenuation associated with its porous structure. Notably, the fabric retained its shielding performance even after six months of ambient exposure, highlighting exceptional environmental stability. This study establishes critical structure–property relationships, revealing that induced porosity, meta-structure effects, large flake size, and optimized surface terminations synergistically enhance EMI shielding. By elucidating the interplay between material parameters and shielding performance, this work provides a foundational framework for designing advanced EMI mitigation technologies, paving the way for scalable, high-performance shielding solutions in next-generation flexible and wearable electronics.

Received 7th July 2025
Accepted 4th August 2025

DOI: 10.1039/d5na00662g

rsc.li/nanoscale-advances

Introduction

Electromagnetic interference (EMI) shielding materials are gaining importance because of the urgent demand for electromagnetic compatibility of modern equipment and protection of living tissue from hazardous radiation.[1–3] It is desirable to have high-performance electromagnetic shields with high EMI shielding efficiency (SE), low thickness and weight, superior mechanical strength and flexibility, and good stability.[4,5] Low-dimensional nanomaterials such as metal nanowires, carbon nanotubes (CNTs), graphene, or surface functionalized atomically thin layer transition metal carbides or nitrides (known as MXenes), offer great potential for bottom–up construction of EMI shielding macrostructures and devices due to their good electrical conductivity and high aspect ratios.[6–10] Among these materials, 2D MXene thin sheets with the formula $Ti_3C_2T_x$ (T = O, OH, F, *etc.*), have garnered attention for producing high-performance EMI shielding materials due to their metallic conductivity and solution processability, resulting from their hydrophilic functional groups (O, OH, F, *etc.*).[11] For instance, vacuum-filtered MXene films with a thickness of 11 μm demonstrated a good EMI SE of 68 dB, resulting in an ultrahigh absolute shielding effectiveness (SSE_T) of 25 863 dB cm^2 g^{-1}, compared to solid metallic copper or stainless steel, with SSE_T values of *ca.* 30 dB cm^2 g^{-1}.[12] In another study, an EMI shielding effectiveness of 92 dB at a thickness of 45 μm in the X-band frequency range (8.2 to 12.4 GHz), was observed, showing exceptional promise for applications in modern smart devices.[12]

[a]*Magnetism Lab, Department of Physics, COMSATS University Islamabad, 44000, Pakistan. E-mail: shahzad.hussain@comsats.edu.pk*

[b]*Polymer Composite Group, Directorate of Science, PINSTECH, Nilore, 44000, Pakistan*

[c]*Department of Chemistry, University College London, UK*

This shielding efficacy of $Ti_3C_2T_x$ MXene films is ascribed to their intrinsic electrical conductivity (4500 S cm^{-1}), numerous surface terminations, and laminate architecture, as supported by the theoretical study by Schultz *et al.*[13] Hence, it is important to optimize and understand correlations between these parameters to design an EMI shield with high shielding effectiveness.

The intrinsic features of $Ti_3C_2T_x$, such as metal-like electrical conductivity, are influenced by a variety of parameters, including defect density,[14] flake size,[15] surface functional groups of synthesized MXene flakes and intercalant type.[16] These parameters also directly affect the oxidation kinetics of the produced MXenes. Dong *et al.*[17] suggested that the surface terminations produced during MXene synthesis, are expected to modulate metal-to-insulator transitions and influence functional properties such as magnetism, Li-ion capacity, mechanical properties, and shielding effectiveness.[18–20] To date, chemical etching of Ti_3AlC_2 (a type of MAX phase with general formula $M_{n+1}AX_n$ where n = 1 to 4, M is an early transition metal, A can typically be a Group 13 or 14 element and X is carbon in this case, but can be nitrogen in other cases) using fluoride-based acids or salts (such as HF and LiF/HCl), has been a simple method for preparing 2D MXene $Ti_3C_2T_x$ (T = O, OH, F). These traditional etching chemicals can react selectively with the Al layer and remove the resulting AlF_3 from the interlayer space and introduce various functional groups.[21] However, it has been noticed that harsh etching conditions in the case of HF (strong acid), can induce additional structural defects in MXenes and promote their degradation to metal oxides such as TiO_2.[22] In contrast, mild etchants such as LiF + HCl, can produce better quality sheets with greater stability of MXene sheets in an aqueous dispersion (Fig. S2). Hence, a comparative investigation is necessary to determine the impacts of either mild or hard etching conditions on the EMI shielding capabilities.

The porosity, flake size and alignment of highly conductive nano-layered structures are expected to have a significant impact on EMI shielding characteristics.[23] Liu *et al.*[24] showed that creating a porous structure between $Ti_3C_2T_x$ nanosheets, can increase *d*-spacing to a greater extent and can significantly reduce stacking of sheets, leading to better attenuation of electromagnetic waves. It is typically possible to acquire the porous morphology of thin films assembled with nanoparticles at the pre-forming or post-treatment stages. Zhao *et al.*[25] obtained a porous structure by incorporating polymethyl methacrylate (PMMA) microspheres between $Ti_3C_2T_x$ nanosheets, which were then removed at 450 °C. Moreover, porous foams and aerogels, as well as segregated structures, have shown improved shielding performance.[26,27] Recently, highly aligned graphene/polymer nanocomposites were found to have significantly improved shielding efficiency.[23] Hence, by controlling the microstructure of multilayered $Ti_3C_2T_x$ thin films, shielding properties can be improved. Thus, while designing MXenes for EMI applications that require high electrical conductivity, porous structure, and dipole losses, careful control over the influencing factors is essential.

In the present work, shielding properties have been investigated for a range of parameters, including etchant type, surface chemistry, flake size, microstructure, thickness, and $Ti_3C_2T_x$ (T = O, OH, Cl, F) loading. The thickness of films was varied to tune the EMI shielding effectiveness over a wide range where 60 dB (99.9999% shielding efficiency) was obtained for a 14 μm film with an excellent absolute shielding effectiveness (SSE_T) of 53 210 dB cm^2 g^{-1}. In addition, a robust, freestanding $Ti_3C_2T_x$ film that underwent heat treatment in an inert environment and had a thickness of only 5 μm, demonstrated an X-band EMI SE of 71 dB, which was approximately 37% higher than that of the pristine film. Thus, it outperforms previous freestanding MXene-based films with an ultrahigh SSE_T value of 72 300 dB cm^2 g^{-1} at comparable thickness, which is attributed to anomalously high absorption of electromagnetic waves due to a significant change in the layered structure (metamaterial-like structure) as evident form SEM studies.

Motivated by the high shielding efficiency results of thin films, cotton fabric (CF) was also chosen as a substrate to coat the conductive dispersion because $Ti_3C_2T_x$ is polar in nature and has a negatively charged surface that supports good adhesion with cellulose $(C_6H_5O_{10})_n$-based fabrics (cotton, linen, *etc.*).[28] CF was coated with two different loadings of $Ti_3C_2T_x$, resulting in a total shielding effectiveness of 82 dB (among the highest for synthetic materials of comparable thickness). The EMI SE was retained even after six months by storing the fabric under ambient conditions (open to air). Both the fabric properties (porosity, high yarn density and weave pattern) as well as the high electrical conductivity and layered structure of the MXene have clearly contributed to the exceptional EMI SE performance. Indeed, the results presented here fulfil all the desired performance criteria for telecommunications, detection systems, defense, and aerospace applications.

Methods

Materials and chemicals

Hydrochloric acid (HCl, 37% purity) was obtained from Riedel-de Haen; lithium fluoride (LiF), and MAX powder (Ti_3AlC_2) were bought from Aladdin Biochemical Technology (Shanghai, China). The non-sterile, hydrophilic PVDF membranes (pore size 0.45 μm) were obtained from Durapore (Fig. S1). Cotton fabric (CF) was bought from the textile industry (The Crescent Textile Mills Ltd). Without any further purification, all reagents were used as it is in the following protocol.

Amalgamation of chemically exfoliated 2D MXene ($Ti_3C_2T_x$) nanosheets

The etching and the delamination procedure of $Ti_3C_2T_x$ nanosheets is shown by a schematic diagram in Fig. 1(a). Minimally intensive layer delamination (MILD), a top–down facile approach was used to prepare a green colloidal dispersion of single delaminated $Ti_3C_2T_x$ sheets.[29] This method is unique as it is easy to process, retains the size and properties of the flakes and expands the production and scalability of the exfoliated $Ti_3C_2T_x$ dispersion. A milder etchant, a combination of HCl +

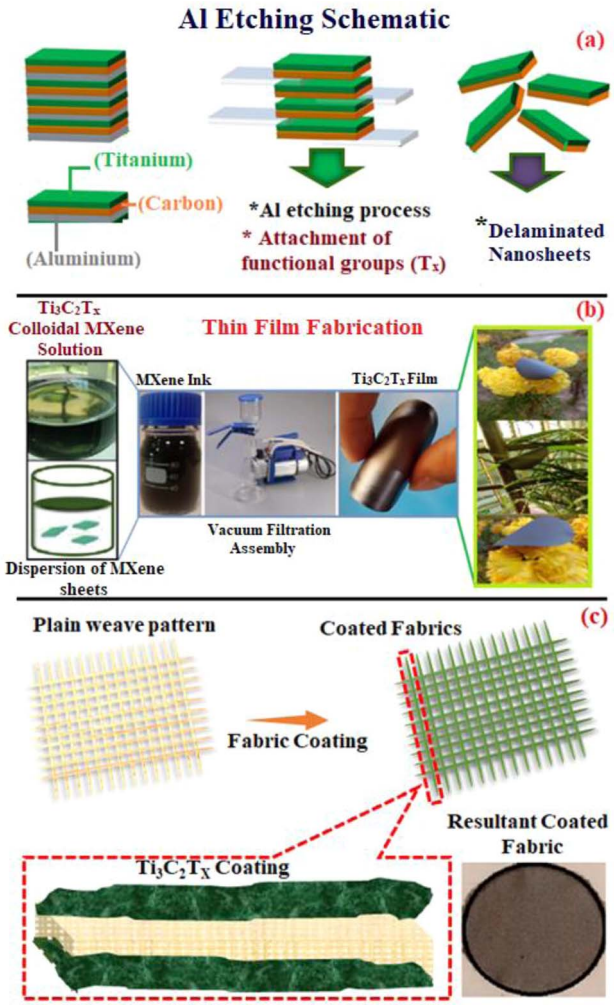

Fig. 1 Schematic illustration of the (a) etching process of the MAX (Ti_3AlC_2) phase and (b and c) fabrication of Ti_3AlC_2 thin films and coating of cotton fabric using a vacuum assisted filtration method. T_x in (a) stands for functional groups which are attached to Ti atoms during the etching process.

LiF, was used for 'Al' etching and successful exfoliation of titanium carbide sheets. In a typical procedure, 3M LiF was added into 37 wt% concentrated HCl in a Teflon-lined beaker and mixed at 400 rpm for 10 min. Then, 2 g of Ti_3AlC_2 was added gradually over 15 minutes into it and the temperature was maintained at 38 °C for 48 h to completely etch the Al layer. The resultant slurry was centrifuged several times with deionized water until the pH value of the supernatant was in the range of 6 to 7. After achieving a neutral pH of the supernatant, the resultant sediments were again diluted with deionized water and sonicated in an ice bath for 1 h to obtain the exfoliated nanosheets. The Ti_3C_2 nanosheet dispersion was again centrifuged at 3500 rpm for 10 minutes to remove impurities. A green colored stable colloidal solution was attained which confirmed the successful etching of 'Al' and exfoliation/delamination of Ti_3C_2 nanosheets.[30]

The chemical reaction during the whole process was as follows:[31]

$$Ti_3AlC_2 + 3LiF + 3HCl \rightarrow Ti_3C_2 + AlF_3 + 3LiCl + (3/2)\,H_2 \quad (1)$$

wherein Ti_3AlC_2 was the MAX powder and LiF and HCl were used as the etchant. H_2 gas was released during the reaction and AlF_3 and LiCl salts were removed during washing, leaving behind suspended multilayer stacked sheets of Ti_3C_2. Hydrofluoric acid (HF) can also be used as an etchant (Fig. S2); however it is a strong acid that can damage the flakes of Ti_3C_2 (Fig. S3). Furthermore, in the next processing step, dimethyl sulfoxide (DMSO) delamination is required to obtain a stable colloidal dispersion.[32] The authors also etched Al using HF acid and fabricated thin films with both LiF + HCl and HF etched solution, to study the effect of different etchants on flake size and consequently, on EMI shielding properties. The details of the HF etching procedure are given in the supplementary data file.

Preparation of freestanding $Ti_3C_2T_x$ thin films

Free-standing $Ti_3C_2T_x$ thin films of different thicknesses were fabricated using a vacuum filtration approach. A substrate, either PVDF filter paper or cotton fabric, was placed on a porous plate of the filtration setup and the Buchner funnel was filled with a specific concentration of the prepared colloidal solution. The vacuum filtration process left the nanoparticles on top of the substrate, while removing the liquid from the colloidal solution, which was then discarded. The obtained $Ti_3C_2T_x$ thin films were dried in a vacuum oven at 60 °C to get thin, flexible, shiny, and light weight films. The filtration assembly and fabricated thin films are shown in Fig. 1(b).

Coating of 2D MXene ($Ti_3C_2T_x$) nanosheets onto cotton fabric

Before coating, the fabric was dried in an oven at 70 °C to remove moisture. The cotton fabric was cut in dimensions of 8.6 × 7.4 cm and then a specific amount of the dispersion was deposited onto it by vacuum filtration. In this case, cotton functioned as a filter membrane while the presence of carboxyl or hydroxyl groups on the surface of cotton helped in the loading of the dispersion. In the next step, only one side of the fabric was coated with half of the dispersion and dried in a vacuum oven for 4 h at 60 °C. When one side was completely dried, then the other side was coated and dried again in a vacuum oven for 4 h at 60 °C. The loaded cotton fabric was still flexible, lightweight, and had good mechanical strength under moderate stretching. The same strategy and conditions were applied to another cotton fabric, which was coated with a different loading. The loading was determined by measuring the total mass before and after coating.

The loading was calculated using the following formula.

$$\text{Loading (mg mL}^{-1}) = \text{mass of coated cotton fabric} - \text{mass of uncoated cotton fabric} \quad (2)$$

Material characterization

The crystal structures of Ti_3AlC_2 and $Ti_3C_2T_x$ were identified through powder X-ray diffraction (XRD) using monochromatic Cu Kα radiation ($\lambda = 1.5405$ Å) using a voltage of 40 kV at a scan

rate of 1° min^{-1} in the scanning angle 2θ range of 0 to 60°. The stability of the $Ti_3C_2T_x$ dispersion was analyzed using a zetasizer nano ZS apparatus (Malvern Panalytical, UK). Dynamic light scattering (DLS) measurements were performed to study the size distribution of 2D $Ti_3C_2T_x$ sheets, by using a backscattered light detector operated at an angle of 173°. The morphology and microstructure of the delaminated/exfoliated $Ti_3C_2T_x$ thin film as well as cotton fabric, was analyzed using a field emission scanning electron microscope (FE-SEM) and EDS measurements were also performed (Fig. S4 and Table S1). The electronic structure was examined by X-ray photoelectron spectroscopy by using an incident beam from an Al X-ray source (1486.5 eV) operated at 10 kV, 10 mA, and 100 W for both survey and high-resolution scans. The EMI shielding properties of $Ti_3C_2T_x$ thin films and cotton-coated $Ti_3C_2T_x$, were measured through a vector network analyzer at room temperature using the waveguide method within 8–12 GHz (X-band). Scattering parameters S_{11} or S_{22} (reflection coefficient data) and S_{12} or S_{21} (absorption coefficient data) were recorded and used to calculate the reflection coefficient (R), absorption coefficient (A), and transmission coefficient (T) as follows.

$$R = |S_{11}|^2 = |S_{22}|^2 \quad (3)$$

$$A = 1 - R - T \quad (4)$$

$$T = |S_{12}|^2 = |S_{21}|^2 \quad (5)$$

The total shielding effectiveness (SE_T), shielding effectiveness due to reflection (SE_R), shielding effectiveness due to absorption (SE_A), attenuation percentage (shielding efficiency) and effective absorption percentage (abs %), can be calculated by using the following formula.

$$SE_T = SE_A + SE_{MR} + SE_R \quad (6)$$

SE_{MR} can be ignored when $SE_T \geq 15$ dB.[33]

$$SE_R = -10\log(1 - R) \quad (7)$$

$$SE_A = -10\log\left(\frac{T}{1-R}\right) \quad (8)$$

$$A_t(\%) = 100 - \left(\frac{1}{10^{(SE_T/10)}}\right) \times 100 \quad (9)$$

$$A_{eff} = \frac{(1 - R - T)}{(1 - R)} \quad (10)$$

For non-magnetic and highly conductive shields, the SE_A and SE_R can be written as

$$SE_R = 50 + 10\log\left(\frac{\sigma}{f}\right) \quad (11)$$

$$SE_A = 1.7t\sqrt{\sigma f} \quad (12)$$

where, σ, t and f are the electrical conductivity, thickness of shield and frequency of electromagnetic waves, respectively. These equations indicate the strong dependence of shielding parameters on electrical conductivity.

Results and discussion

Zeta potential and dynamic light scattering measurements (DLS) were performed to examine the colloidal properties of $Ti_3C_2T_x$ nanosheet dispersions as shown in Fig. 2. $Ti_3C_2T_x$ flake dispersions in water showed colloidal stability and homogeneity without the addition of any surfactant, at pH values ≥6. The stability and homogenous suspension of $Ti_3C_2T_x$ flakes in water are due to the negatively charged Ti_3C_2 nanosheets, which are induced by the presence of functional groups (*e.g.*, OH, F, and Cl). In particular, F and Cl anions are highly electronegative, making the surface of sheets more negative.[34] Fig. 2(a) shows that the aqueous $Ti_3C_2T_x$ mixture (pH value ≥6) had a large negative zeta potential of −32.1 mV, which confirmed the colloidally stability of the Ti_3C_2 nanosheet dispersion due to electric double layer compression.[35] Fig. 2(b) on the hand shows the variation of zeta potential indicating a large negative potential with increased pH. Under acidic conditions, the low zeta potential caused flocculation of $Ti_3C_2T_x$ flakes (suspension physically unstable) due to weak repulsive charge that was not sufficient to overcome van der Waals attractive forces.[36] Thus, the dispersion was maintained at pH values ≥6. Higher colloidal stability was also observed for $Ti_3C_2T_x$ nanosheet suspensions that were made by etching with mild acid (LiF + HCl) as compared to strong hydrofluoric acid (Fig. S2(a) and (b)).

Flake size is known to be a crucial factor affecting the electrical conductivity of a system, which in turn determines its EMI shielding properties.[37] The larger the flake size, the better will be the contact between the flakes, and the higher will be the conductivity.[37] Fig. 2(c) shows the DLS flake size distribution of $Ti_3C_2T_x$ nanosheets with an average flake size of *ca.* 615 nm. As discussed in the zeta potential studies, the degradation mostly occurred at the edges of nanosheets, which was linked to the size of the flake and was most pronounced for small flakes. It was also shown that large flakes of $Ti_3C_2T_x$ formed more stable dispersions.[34,38] Larger flake sizes were observed after the LiF + HCl treatment as compared to HF acid treated solutions (Fig. S3) and both dispersions were used for thin film fabrication. The small peak in the size distribution data in Fig. 2(c) not only gives information about the size of small flakes, but also demonstrates the size of solvent molecules *i.e.*, water or the thickness of the nanosheets. Based on the working principle of DLS, the incident light falls on the surface or edges of the flakes and scatters to give information about the average flake size as well as their thickness.[39] The Tyndall effect was distinctly visible, displaying a uniform and stable, well (or evenly) dispersed green-colored $Ti_3C_2T_x$ colloidal solution in water because of terminal surface functional groups *e.g.*, OH, F, Cl, *etc.*[40,41]

Fig. 3(a) shows the diffraction patterns of the parent MAX powder (Ti_3AlC_2) and M5 (5 μm) free standing $Ti_3C_2T_x$ films (both without and after heat treatment); the data were taken at room temperature in the 2θ range of 5 to 65°. The characteristic

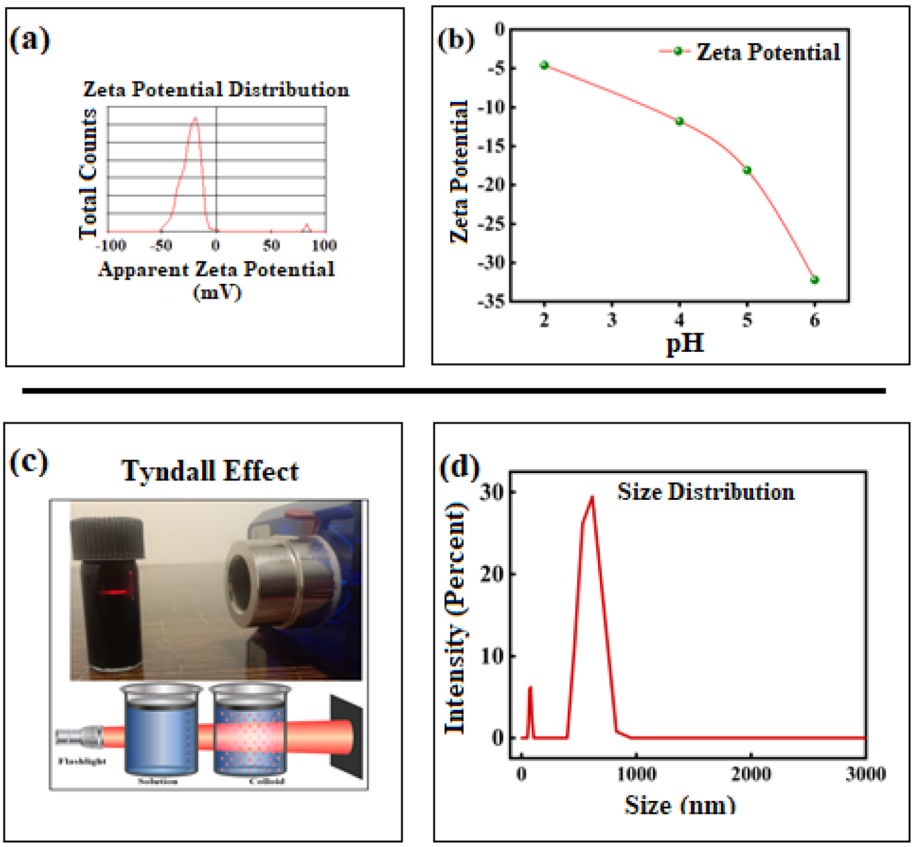

Fig. 2 Zeta potential of (a) $Ti_3C_2T_x$ supernatant at pH ~ 6, (b) zeta potential as a function of pH, (c) shining of a laser into the well dispersed colloidal suspension showing scattering of the beam of light by colloidal particles (Tyndall effect), (d) zeta size distribution of $Ti_3C_2T_x$ supernatant at pH ~ 6.

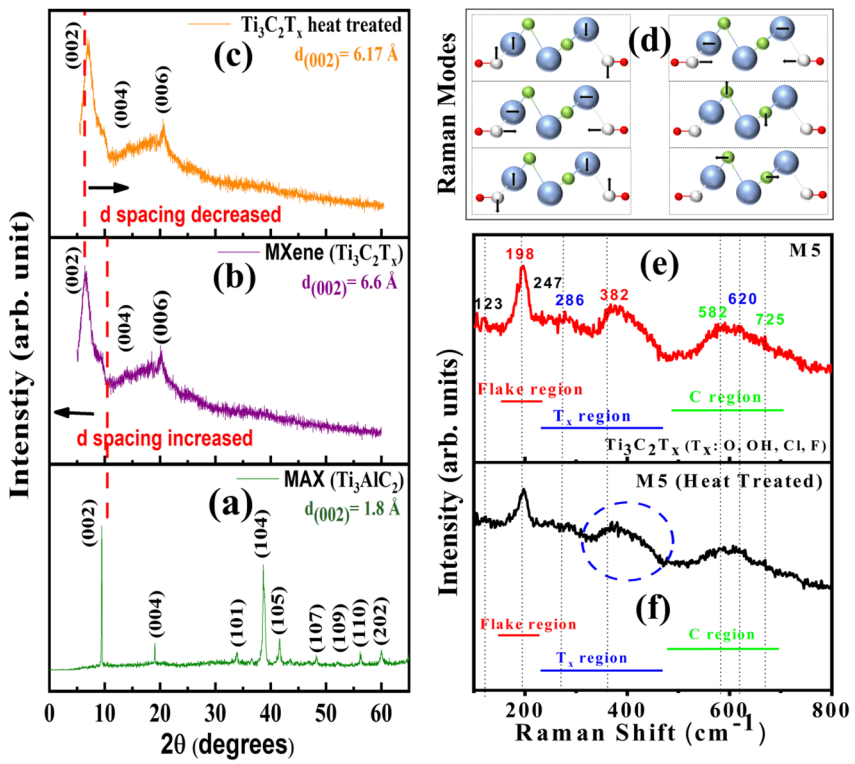

Fig. 3 XRD plots of the Ti_3AlC_2 MAX phase (a), exfoliated $Ti_3C_2T_x$ (b) and heat treated $Ti_3C_2T_x$ (c) films. Raman spectra of $Ti_3C_2T_x$ (M5) thin films before (e) and after (f) heat treatment (both measured at room temperature). (d) Various vibrational modes of $Ti_3C_2T_x$ where blue, green, red, and white represent Ti, C, and functional groups (T_x), respectively.

diffraction peaks of Ti_3AlC_2 were located at 2θ values of 9.4°, 19°, 34°, 38°, 41.6°, 48.3°, 56.1° and 60.1° corresponding to (002), (004), (101), (104), (105), (110) and (202) planes, consistent with the literature.[42] After eliminating the Al layer, the diffraction pattern of $Ti_3C_2T_x$ was free of almost all diffraction peaks of Ti_3AlC_2 except the (002) peak at $2\theta \approx 6°$, indicating successful etching of Al atoms. Moreover, the appearance of small diffraction peaks corresponding to (004), and (006) planes, indicates the multilayer nature of $Ti_3C_2T_x$ films.[43] Hence, the selective extraction of 'Al' atoms from Ti_3AlC_2 when using a mild etchant mixture of HCl and LiF for 48 h, ensured a successful transition from the block multilayer structure of Ti_3AlC_2 into the accordion-like layered structure of $Ti_3C_2T_x$ as shown in Fig. 3(b). Furthermore, the (002) diffraction peak became broader, weaker, rougher, and shifted to lower angles, from 9.4° to 6° in 2θ, after the etching process.[44] This shift may be attributed to the formation of Ti_3C_2 basal planes and an increase in the interlayer *d*-spacing from *ca.* 1.8 to 6.6 Å along the [0001] direction (an increment in the *c*-axis). The expansion of *d*-spacing was due to the presence of intercalants and an increase in the spacing between $Ti_3C_2T_x$ flakes.[12,40] Moreover, some functional groups, T_x (OH, F, or Cl) might have been attached to the surface or edges of Ti_3C_2 nanosheets. These results suggested successful etching of Ti_3AlC_2 as well as the exfoliation/delamination of $Ti_3C_2T_x$.[45,46] The same film was annealed at 300 °C for four hours to understand the effects of temperature on the internal structure and on EMI shielding properties. A slight increase in 2θ values was observed, indicating a decrease in interplanar spacing due to the removal of functional groups.

The information regarding the surface chemistry, stacking, and quality of $Ti_3C_2T_x$, was obtained using Raman spectroscopy. Fig. 4(e) and (f) compares the Raman shift, revealing characteristic peaks at wavenumbers associated with $Ti_3C_2T_x$ vibrations, and their respective surface functionalization for $Ti_3C_2T_x$ films, before and after heat treatment. The vibrations of $Ti_3C_2T_x$ consisted of E_g (in-plane) and A_{1g} (out-of-plane) peaks from both Ti and C atoms, consistent with the literature.[47] The spectrum was divided into three regions; (i) the flake region, which represented group vibrations of carbon, two titanium layers, and functional groups, (ii) the T_x region, which denoted surface group vibrations and, (iii) the carbon region (C region) that included both in-plane and out-of-plane vibrations of the carbon atoms. The A_{1g} peaks at 198 cm^{-1} and the E_g peaks at 247, 286, and 382 cm^{-1} represent vibrations caused by titanium surface groups. The carbon vibrations were represented by the E_g and A_{1g} peaks at *ca.* 582/620 cm^{-1} and *ca.* 725 cm^{-1}, respectively.[48,49] The broadening and merging of lines in the spectra indicated that the Ti_3AlC_2 precursor had undergone exfoliation and delamination.[48] The different Raman modes of $Ti_3C_2T_x$ are shown in Fig. 3(d). The vibrations of the free-standing film before and after heat treatment matched the peaks at 123, 198, 247, 286, 382, 582, 620, and 725 cm^{-1}; however, there were some slight variations in the peak intensities. The partial elimination of functional groups was observed upon annealing at a higher temperatures in the range of 350 to 480 cm^{-1}.[48] Hence, a slight variation in the overall peaks was noted after heat treatment, but the characteristics of the respective functional groups remained the same. It was suggested that some of the OH functional groups had

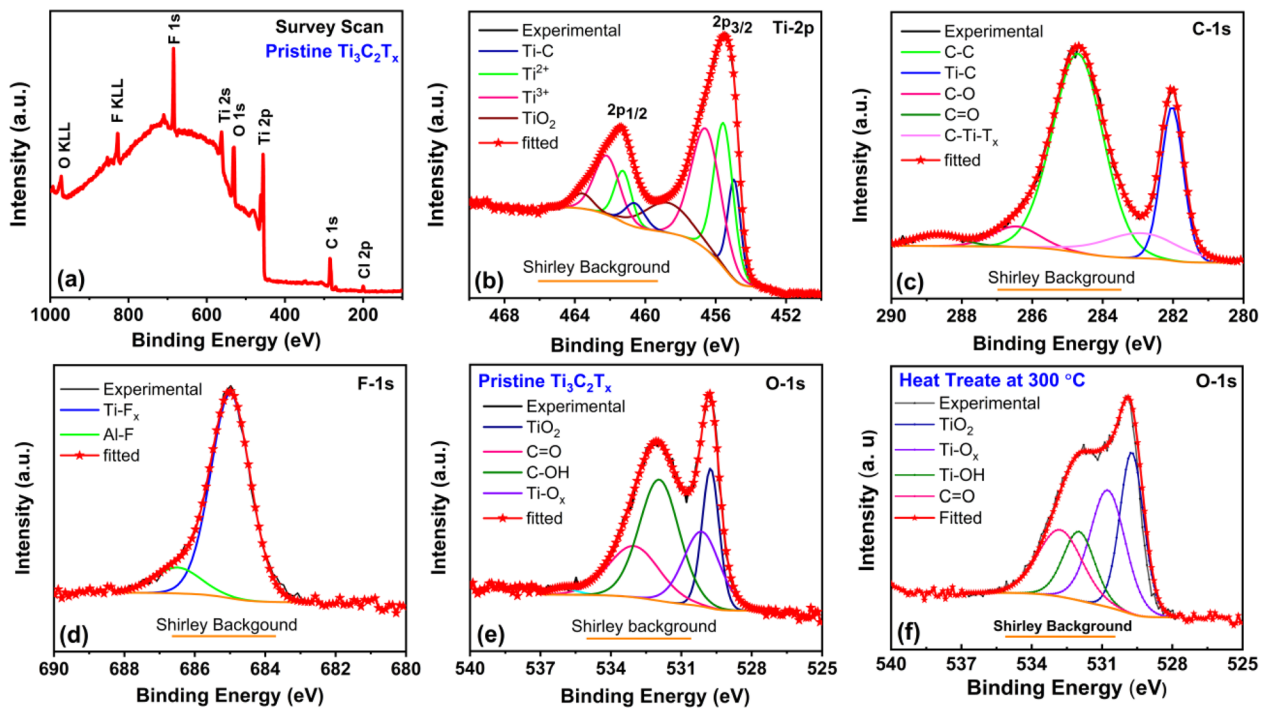

Fig. 4 X-ray photoelectron spectroscopy results of $Ti_3C_2T_x$ films measured at room temperature. (a) Survey scan, and high-resolution scans of (b) titanium, (c) carbon, (d) fluorine and (e) oxygen and (f) oxygen region of heat-treated films. The fitting is done with Shirley background.

a propensity to transform into oxide (O) increasing the mechanical stability of the membrane and decreasing the *d*-spacing.[50] Heat treated and subsequently dried films maintained their chemical stability, allowing them to be stored in an ambient environment (in air) for extended periods of time.

X-ray photoelectron spectroscopy (XPS) was used for determining the surface chemical compositions, atomic bonding, and chemical states of delaminated $Ti_3C_2T_x$ films. Fig. 5(a) shows the survey scan of the M5 free standing thin film, which revealed a series of sharp peaks corresponding to direct excitation of electrons from core levels in Ti, C, O, F, and Cl. The O-KLL and F-KLL peaks were obtained due to Auger electrons and the absence of the Al peak indicated the successful etching of Al during the synthesis process.[32,51,52] Fig. 5(b)–(f) shows high resolution scans of various elements (Ti 2p, C 1s, O 1s, and F 1s) incorporated during exfoliation which were de-convoluted in different peaks using CasaXPS with asymmetric Gaussian–Lorentzian curves. The surface chemistry of $Ti_3C_2T_x$ MXene improved the polarization of local dipoles.[53] The systems were also characterized by FTIR spectra and the data for M5 sample are shown in Fig. S5.

Fig. 4(b) shows the high-resolution core level scan of the Ti 2p region, where spin orbit coupling resulted in two peaks with a 2 : 1 intensity distribution between $2p_{3/2}$ and $2p_{1/2}$ peaks, respectively.[54] The Ti 2p spectrum was deconvoluted into five peaks, each of which was related to Ti–C (Ti^{+1}), Ti–X (Ti^{2+}), Ti–O_y (Ti^{3+}) and TiO_2 (Ti^{4+}). These peaks showed that there were many combinations of terminal groups on $Ti_3C_2T_x$, corresponding to different oxidation states of Ti. The peak positions and other fitting parameters are given in Table 1, which are consistent with the literature.[12,30,55–57] Fig. 5(c) shows the C 1s XPS spectrum, which was fitted with five peaks namely Ti–C, C–C, C–O,

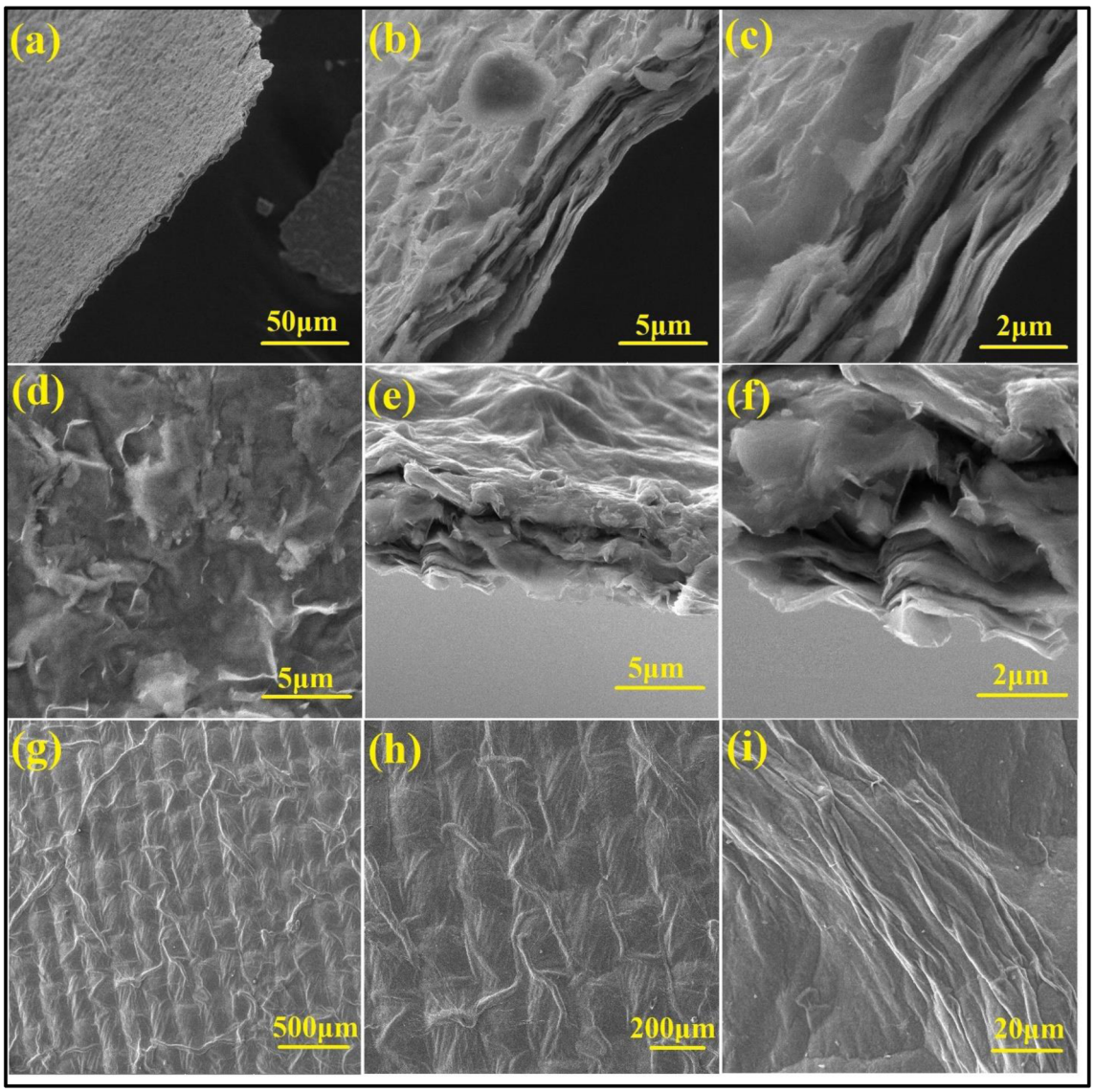

Fig. 5 (a–c) Cross-sectional FE-SEM images of thin film M5, (d–f) surface and cross-sectional images of the heat-treated thin film and (g–i) coated cotton fabric MX20 at three different resolutions.

Table 1 XPS peak fitting results of various regions of the $Ti_3C_2T_x$ sample

Region	B.E (eV)		Assigned to
	$2P_{3/2}$	$2P_{1/2}$	
	454.98	460.68	Ti–C
	455.58	461.28	Ti^{2+}
	456.68	462.28	Ti^{3+}
Ti 2p	458.88	463.58	TiO_2
C 1s	281.98		Ti–C
	282.98		C–Ti–T_x
	284.68		C–C
	286.48		C–O
	288.68		C=O
F 1s	684.98		Ti–F_x
	686.48		TiO_2–F_x
O 1s	529.78		TiO_2
	530.18		Ti–O_x
	531.98		Ti–OH
	533.08		Ti–H_2O
O 1s (heat treated sample)	529.78		TiO_2
	530.78		Ti–O_x
	531.98		Ti–OH
	532.88		Ti–H_2O

C=O, and –CH_x whose binding energy values are given in Table 1. Fig. 4(d) shows the scan spectrum of F 1s, which was fitted with components corresponding to Ti–F_x and Al–F bonds, with binding energy values shown in Table 1. All peak positions assigned to specific bonds were consistent with the literature.[58–62]

Fig. 4(e) and (f) presents O 1s scans of pristine and heat treated $Ti_3C_2T_x$ thin films. The O 1s spectrum was fitted with five peaks that were attributed to the distinguishing bonds TiO_2, TiO_x, C–OH, and C=O. Ti–O_x played a vital role in the stability of the film and prevented its oxidation due to the presence of O_x groups in Ti–O_x that could repel O_2 molecules present in the air. It can be clearly seen that the intensity of the Ti–O_x peak increased, whereas the intensity of C–OH peak decreased for the heat treated $Ti_3C_2T_x$ thin film, indicating the conversion of –OH function groups to oxide (O) groups.[50] Hence, the presence of more O-related states on the surface of the heat treated $Ti_3C_2T_x$ thin film, compared to the pristine $Ti_3C_2T_x$ thin film, led to higher mechanical stability and oxidation resistance of the former. The XPS results were also consistent with the Raman and XRD results, where the authors noted changes in the functional group region of the Raman spectrum and a forward shift of the (002) diffraction peak, indicating a decrease in *d*-spacing due to the removal of functional groups.

Fig. 5(a)–(c) shows the FE-SEM micrographs of $Ti_3C_2T_x$ thin films (M5) after exfoliation at three different magnifications. The cross-sectional images of $Ti_3C_2T_x$ thin films confirmed an accordion-like structure, indicating the typical nanosheet morphology after the removal of 'Al' between the Ti_3C_2 sheets. The distance between nanosheets was larger due to weak van der Waals interaction among layers and the average thickness of a sheet was about 0.20 μm, whereas the total thickness of the film was 5 μm. The accordion like morphology of $Ti_3C_2T_x$ thin films made the system more favorable for multiple scattering and the brightness of the layers indicated that the film was highly conductive. The highly electrically conductive $Ti_3C_2T_x$ multiple layers formed conductive paths and were arranged in parallel positions, as shown in Fig. 6, which indicated that the system was anisotropic.[63] Fig. 5(d)–(f) shows the morphology of the heat treated M5 thin film prepared at 300 °C in an inert environment for four hours. The heat treatment led to significant changes in the layered structure, making it more porous with many interstices, sites, or defects where there would be a high probability of attenuation of EM radiation.

Fig. 5(g)–(i) shows the surface SEM micrographs of fabricated cotton fabric (CF) with a 1.56 mg cm^2 loading of $Ti_3C_2T_x$. The micrographs indicated that the coating of $Ti_3C_2T_x$ was uniform with no damage to the weft yarn arrangement of the plain weaving of the cotton fibers. The coating created a conductive path through electrostatic forces, leading to a bright and shiny surface on the fabric as shown in Fig. 5(g)–(i). As cotton fabric dries faster than the layers of deposited $Ti_3C_2T_x$, this results in the formation of wrinkles on its surface due to compressive stress. The surface of the coated CF was rough and at points of interleaving, the direction of yarn was different, which led to irregularities in the fabric and made the system anisotropic. To study the elemental and chemical composition of $Ti_3C_2T_x$ thin films, EDS measurements were performed (Fig. S4). No 'Al' peak was observed in the EDS spectrum of the $Ti_3C_2T_x$, which confirmed the successful etching of 'Al' layers. It is evident from the EDS spectrum that all the expected elements such as Ti, C, and T_x (–OH, –F, –Cl, and –O) were present with atomic ratios given in Table S1. The EDS results could not provide detailed information especially for the –OH group because H cannot be detected by EDS.[37,64] We also observed the presence of Cl functional groups which might play an important role in conducting properties.[65]

Considering the good electrical conductivity of $Ti_3C_2T_x$ thin films, the EMI shielding response of free-standing thin films of various thicknesses was investigated in the frequency range of 8.4 to 12.4 GHz (X-band) as shown in Fig. 6. To study thickness dependent shielding properties, a set of free-standing thin films with different thicknesses named M5 (5 μm thick), M7 (7 μm), M9 (9 μm), and M13 (13 μm) were prepared by the vacuum-assisted filtration method. The variation in different shielding parameters of $Ti_3C_2T_x$ thin films, is shown in Fig. 7(a)–(f) as a function of X-band frequency. The 5 μm-thick film had a maximum SE_T of 45 dB (Table S2), which increased to 60 dB for the 13 μm thick film. SE_A also showed the same trend; it increased with thickness and reached 46 dB for the 13 μm film. SE_A was proportional to the thickness of the shield, which indicated that higher thicknesses led to increased path length, leading to greater attenuation of the electromagnetic waves (eqn (12)). The layered structure of $Ti_3C_2T_x$ thin films as evidenced by FE-SEM images (Fig. 5), was obviously useful for trapping electromagnetic waves as the thickness of the shield increased. The highest SE_T of M13 corresponded to the highest attenuation

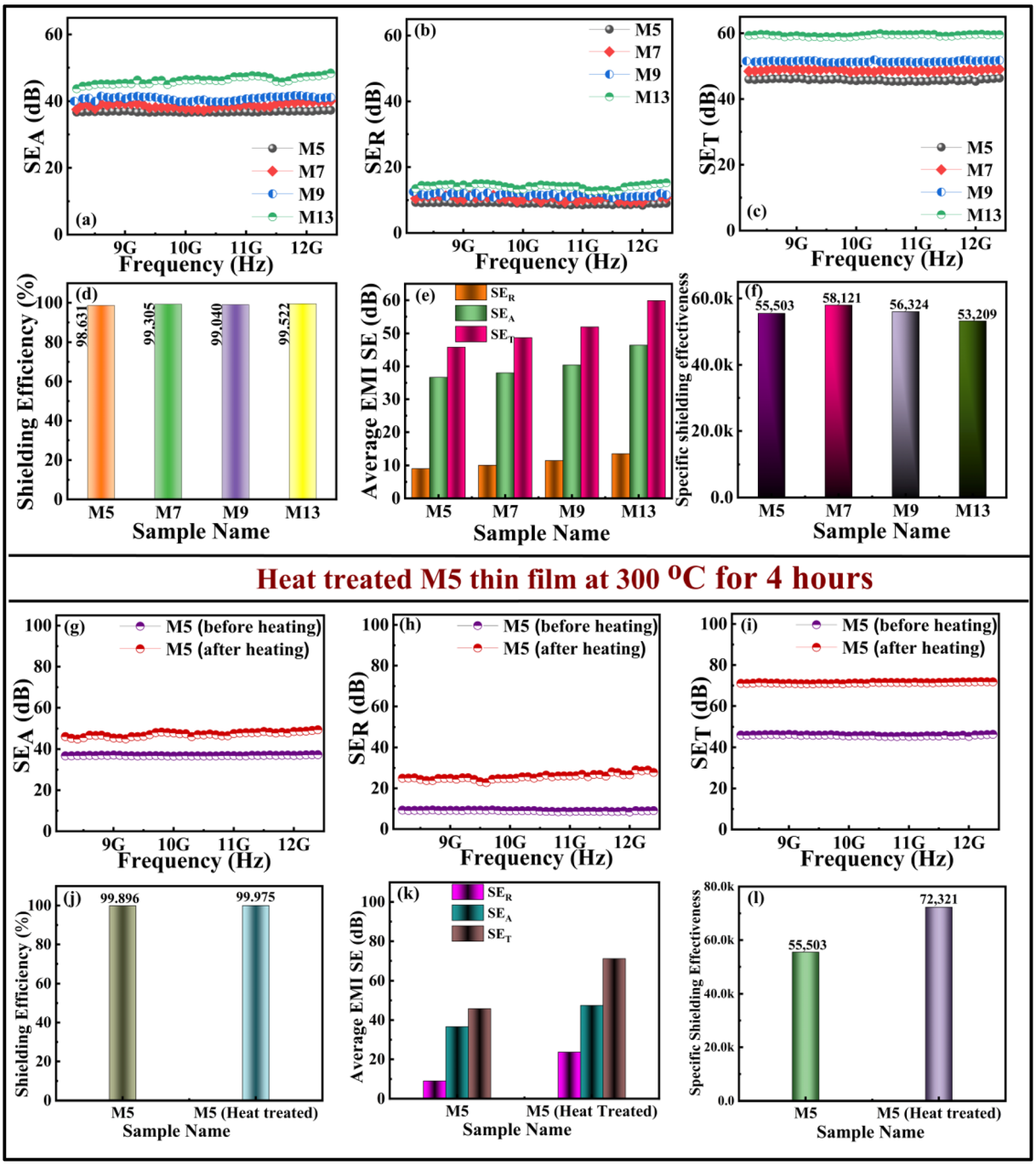

Fig. 6 (a) Shielding effectiveness due to absorption, (b) reflection, (c) total, (d) attention percentage, (e) absorption effectiveness percentage, and (f) absolute shielding effectiveness of M5 (5 μm thick film), M7, M9, and M13. (g–l) Shielding parameters of the M5 thin film after heat treatment as a function of frequency in the X-band.

of 99.999% and an effective absorption of 99.99%, respectively, as shown in Fig. 7(d). The results suggested that the layered structure of $Ti_3C_2T_x$ displayed absorption-dominant phenomena. Moreover, the SE_A part was also prominent due to the presence of functional groups, excess charge carriers, and dipolar polarization, as shown in Fig. 7(a). SE_R hardly changed for all $Ti_3C_2T_x$ films and remained around 9–12 dB, indicating that the difference in SE_T was mostly caused by SE_A; indeed, it is known that SE_R values are mainly determined by impedance mismatches.[3] The low value of SE_R also makes this study important as most of the studies in the literature have reported values well above 20 dB.[66,67] Thus, EMI shielding results indicated that the high electrical conductivity, dipolar polarization, and layered structure of the MXene sheets were crucial factors that determined the remarkable EMI shielding performance.

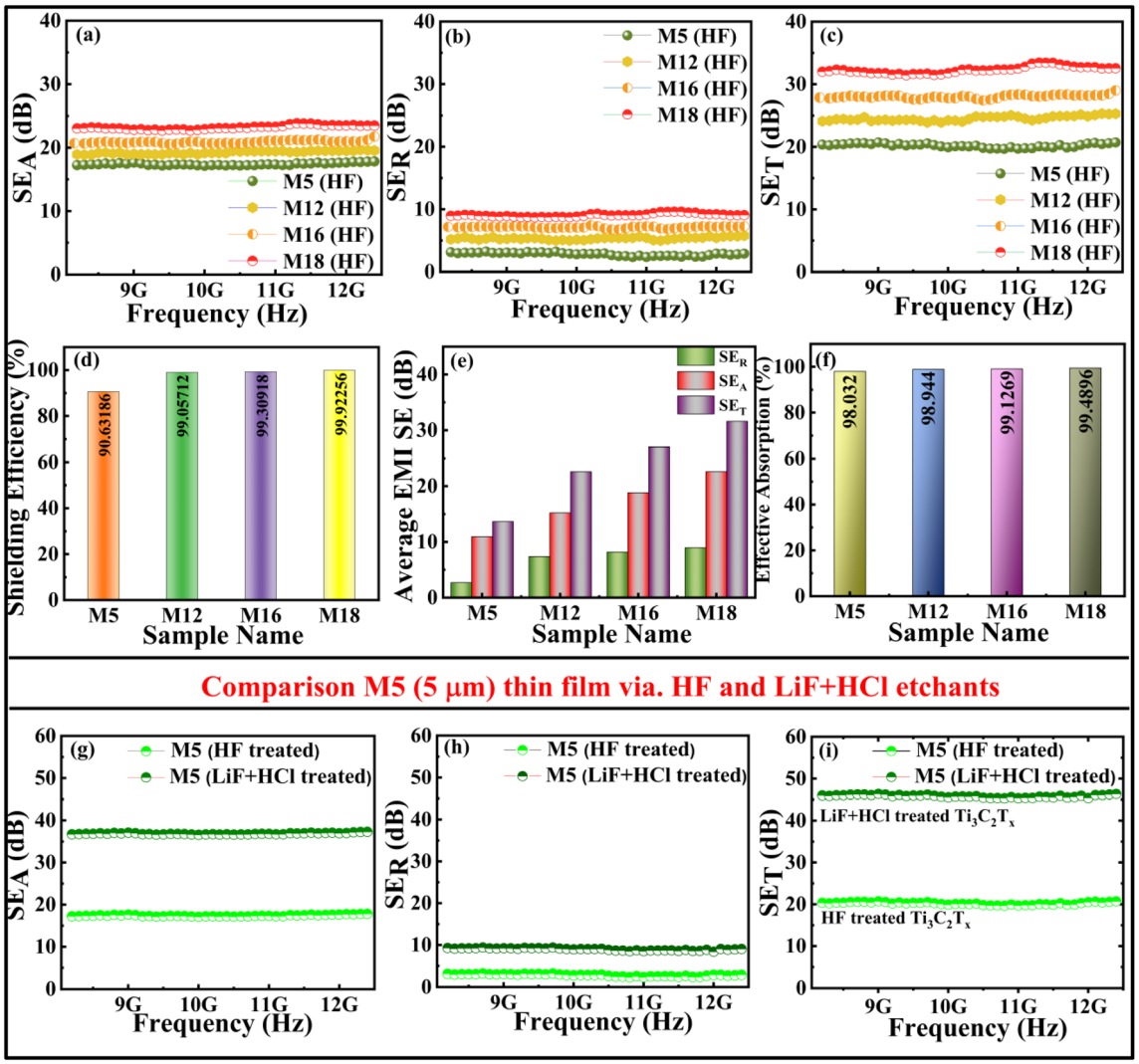

Fig. 7 (a–i). Comparison of EMI shielding parameters using HF etched and LiF + HCl etched $Ti_3C_2T_x$ dispersions. (a) Shielding effectiveness due to absorption, (b) reflection, (c) total shielding effectiveness, (d) shielding efficiency, (e) average EMI SE, and (f) effective absorption of M5(HF treated and 5 μm thick), M12(HF), M16(HF), and M18(HF) thin films using HF etched $Ti_3C_2T_x$ dispersion in the X-band. (g–i) Comparison of M5 thin films.

As the shielding properties are strongly related to the layered structure of $Ti_3C_2T_x$ thin films, heat treatment of M5 thin films was performed at 300 °C for four hours in an inert environment of N_2 gas (designated as M5HT). The heat treatment was expected to modify the microstructure of film and tune functional groups. A significant increase of 26 dB was observed in SE_T (71 dB) as shown in Fig. 6(i). The authors observed, as shown in Fig. 6(g), that this increase in SE_T occurred due to enhanced absorption as well as reflection, as evidenced by the high values of SE_A and SE_R. Also, it was noted, as shown in Fig. 5(e) and (f), that the layered structure, and porous nature became more prominent after the heat treatment. This microstructural change was mainly responsible for the significantly high value of SE_A. SE_R also increased from 9 dB to 23 dB, which suggested that along with the microstructural changes, there was also a change in conductivity of the film, which led to increased mismatch and more reflection. This conductivity increase was ascribed to the removal of adsorbed water molecules and surface terminations, leading to a decrease in *d*-spacing as confirmed by XRD studies. However, the maximum contribution to the total shielding effectiveness was still due to absorption, which is preferable in $Ti_3C_2T_x$ free-standing thin films to avoid secondary pollution. Regardless of film thickness, the EMI SE of all the films studied in this work were well above 20 dB, meeting the requirement for practical commercial applications.

We conducted electrical conductivity measurements on different thin film samples and the outcomes are in alignment with both the flake size and the surface functional groups. As described, the –F terminations tend to improve electron confinement due to the high electronegativity of fluorine, which lowers conductivity. On the other hand, –OH and –O groups improve electron transport, thus enhancing conductivity as shown in Fig. 9(c). Regarding HF-etched samples, the more

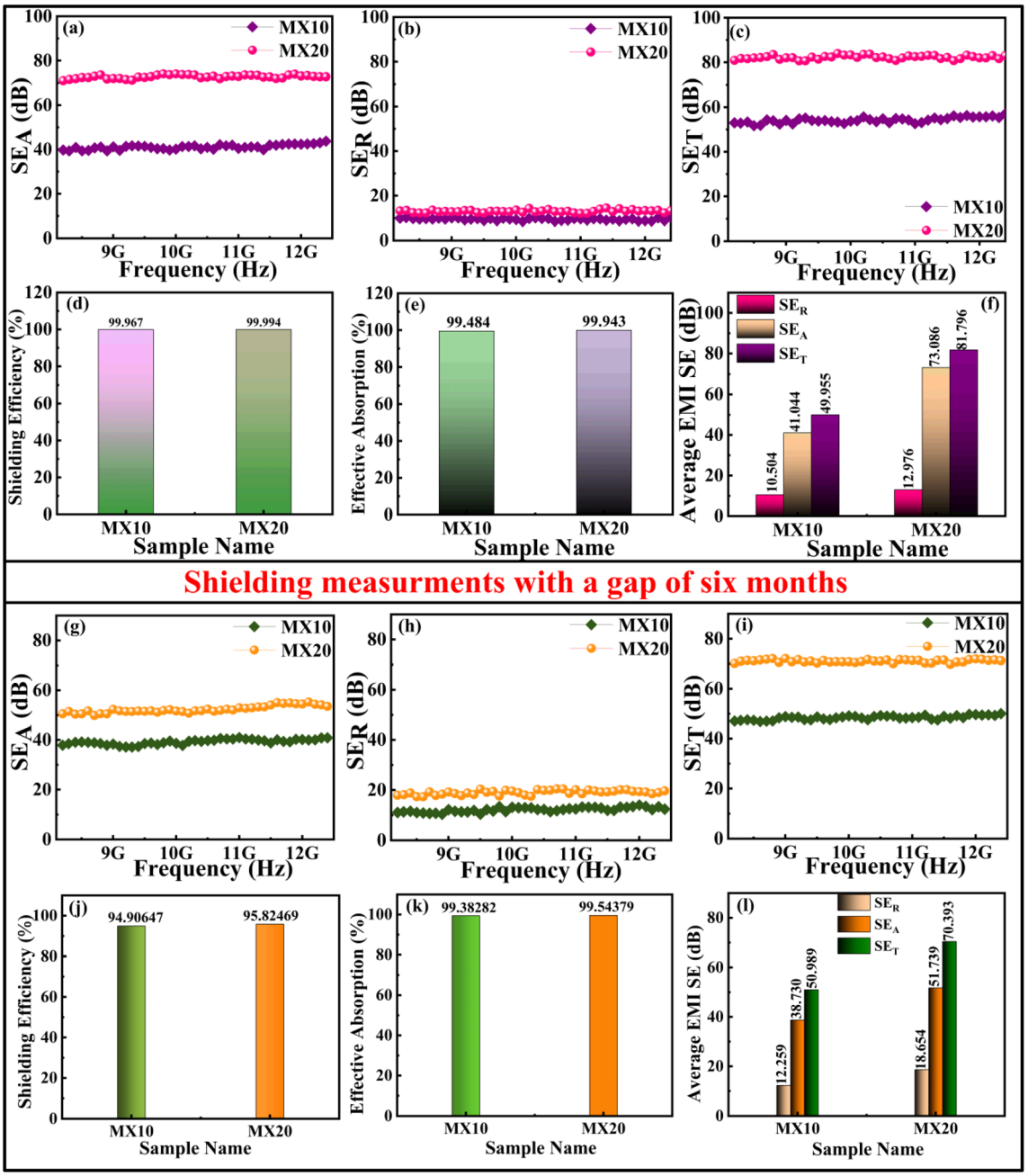

Fig. 8 (a–l) (a) Shielding effectiveness due to absorption, (b) reflection, (c) total shielding effectiveness, (d) attention percentage, (e) absorption effectiveness percentage, and (f) average EMI shielding effectiveness of MX10 (0.8 mg cm^{-2}) and MX20 (1.6 mg cm^{-2}) in the X-band. (g–l) Shielding parameters after a gap of six months.

aggressive etching increases the etch rate of the flakes, which leads to smaller flake sizes (Fig. S2), resulting in greater flake boundary and interface density. This increased boundary density leads to scattering of charge carriers, which decreases conductivity. For the samples that underwent heat treatment, a substantial increase in conductivity was observed. The increases are likely due to be higher ordering of the structure and interflake connections. Increased heat treatment likely increases the interflake contacts and decreases the surface defects, thus improving the charge transport and EMI shielding performance.[68]

Specific shielding effectiveness (SSE) and absolute shielding effectiveness (SSE_T) are key parameters to evaluate the EMI shielding efficiency of $Ti_3C_2T_x$ with different densities and thicknesses. Increases in thickness, density, and mass of films can affect the performance and efficiency of the shielding material. The SSE and SSE_T are given by eqn (13) and (14), respectively, and can be used to perform a comparative analysis of the intrinsic shielding properties of different specimens.

$$\mathrm{SSE}\left(\mathrm{dB\ cm^3\ g^{-1}}\right) = \left(\frac{\mathrm{SE}_T}{\mathrm{density}}\right) \quad (13)$$

$$SSE_T\left(\text{dB cm}^2\ \text{g}^{-1}\right) = \left(\frac{\text{SSE}}{\text{thickness}}\right) \quad (14)$$

The calculated values of SSE and SSE_T for M5, M7, M9, and M13 are listed in Table S2 together with their respective thicknesses. The table also shows a literature comparison of these quantities measured on similar systems. The SSE_T for M5 is 55 503 dB cm^2 g^{-1}, which increased to 58 121 dB cm^2 g^{-1} for the M7 sample. A significant increase in SSE_T was observed for the heat treated M5 sample, where the SSE_T reached 72 321 dB cm^2 g^{-1}. This to the best of our knowledge is the highest value of SSE_T for $Ti_3C_2T_x$ thin films having a thickness of only 5 μm. The high EMI SE of the prepared samples is attributed to the accordion like layered structure of $Ti_3C_2T_x$ (see Fig. 9(b)), which caused multiple internal reflections of incident EM radiation, and its excellent conductivity, which provided abundant free electrons to scatter and absorb the energy of the incident EM radiation. The attached functional groups were responsible for the formation of dipoles (Ti^+ and $OH^-/F^-/O^-/Cl^-$) which were also responsible for the absorption of EM radiation as shown in Fig. 9(a).

Regulating the etching conditions of Al can affect conductivity, stability, and EMI shielding properties of $Ti_3C_2T_x$ thin

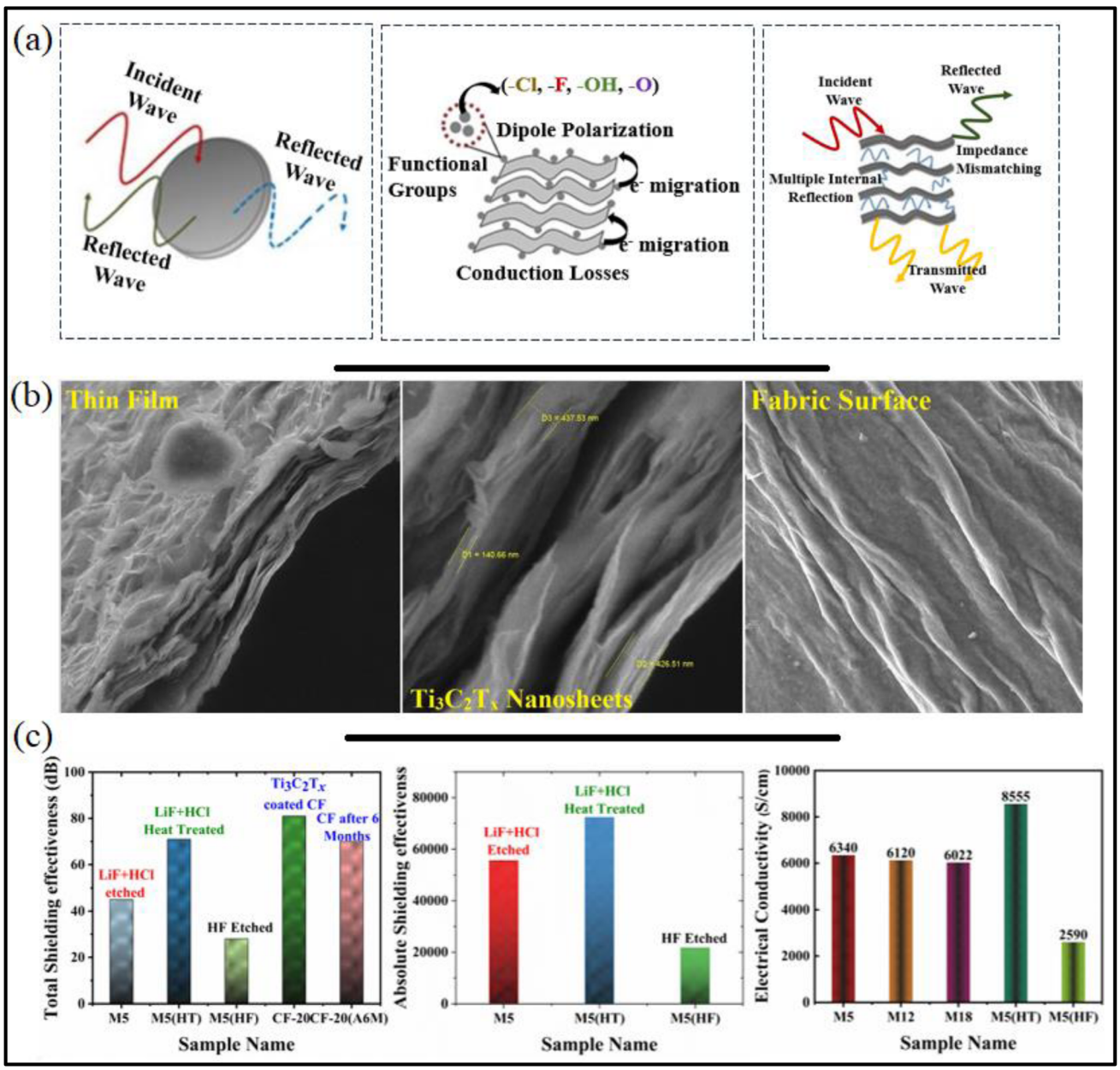

Fig. 9 (a) Schematic diagram of shielding mechanism of $Ti_3C_2T_x$, (b) accordion like morphology of thin films (left and middle figures show film, and the right figure shows the coated cotton fabric) facilitating multiple reflections, and (c) comparative shielding analysis of $Ti_3C_2T_x$ thin films under different conditions and coated fabrics and their conductivity response.

films. The X-ray diffraction data, EDS spectrum, zeta-sizer results and EMI shielding measurements for films (having different thickness) prepared using HF etched dispersion, are shown in the supplementary information. A comparison of EMI shielding properties of 5 μm films prepared using LiF + HCl (M5) and HF (M5HF) etched dispersions, is shown in Fig. 7. The SE_T for M5HF (5 μm film obtained using HF etched dispersion) was 20 dB, which was significantly smaller than that for the M5 (the one obtained from LiF + HCl treatment) film having the same thickness. It is known that the shielding properties of thin films are strongly dependent on the flake size, conductivity, type of surface terminations and microstructure.[69] The average flake size of $Ti_3C_2T_x$ nanosheets obtained by minimally intensive layer delamination (MILD) using LiF + HCl as etchants was 615 nm, which reduced to 220 nm in the case of the HF treated system as shown in Fig. S3. The film with large flake size had a large surface area and more surface terminations, which functioned as electric dipoles and provided better connectivity between sheets, leading to much better conductivity, and shielding properties as shown in Fig. 7(a)–(f). The flake size also influenced the stability of dispersions, as smaller sized flakes showed lower stability compared to larger flakes as shown in Fig. S2(a) and (b). According to theoretical studies, the kind and number of surface terminations have a significant influence on the electrical structure and physicochemical properties of MXenes.[70] It was found that $Ti_3C_2T_x$ films prepared using HF etched dispersion had F as the leading terminations, while films prepared using LiF + HCl etched dispersions contained a larger number of oxide (O) terminations (Table S1). Oxide terminated MXenes are predicted to exhibit higher electrical conductivity compared to F terminated surfaces.[69] Hence, –OH and –O functional groups contribute to improved electrical conductivity by offering better electron delocalization and interflake coupling, which enhances charge carrier mobility.[71] Also, high –F content as a functional group also decreases interfacial polarization which negatively impacts the EMI shielding response due to a decrease in dielectric loss.[12] These differences in terminal groups have also been observed in the study by Hope *et al.*[65] with HF and Li + HCl as etchants. Hence, larger flake sizes led to better conductivity and more functional groups that can induce dielectric loss and lead to good EMI shielding performance in the case of $Ti_3C_2T_x$ thin films prepared using the minimally intensive layer delamination (MILD) method (with LiF + HCl as etchants).[12]

Keeping in view the excellent EMI shielding performance of $Ti_3C_2T_x$ thin films, highly conductive $Ti_3C_2T_x$ coated fabrics were also fabricated. Cotton fabric (CF) was chosen as a substrate to coat the dispersion because the $Ti_3C_2T_x$ is polar in nature and had a negatively charged surface, which adhered well with cellulose $(C_6H_5O_{10})_n$-based fabrics (cotton, linen, *etc.*). The fabric that had been used had high yarn density as well as high porosity. Moreover, the weave pattern of the fabric was ordered in such a way that offered less resistance and supported smooth adhesion of the $Ti_3C_2T_x$ dispersion with the fabric which further increased the conductivity of the coated fabric (Fig. 1(c)). Two samples with 0.8 and 1.6 mg cm^{-2} (designated as MX-10 and MX-20, respectively, with loadings of 10 and 20 mg over an area of 12.57 cm^2) of $Ti_3C_2T_x$ loading were prepared by using vacuum assisted filtration. Fig. 9 shows the comparison of the shielding parameters of MX-10 and MX-20. SE_T of MX-10 was 50 dB throughout the X-band range of frequency, which increased to 82 dB for MX-20. This increase in SE_T of the MX-20 sample was attributed to high loading of $Ti_3C_2T_x$ nanosheets, providing a more effective material for attenuation. A slight decrease in SE_R and a significant increase in SE_A were observed at MX-20. Both samples showed good attenuation (>99.99%) of the incoming EM radiation which further confirmed that the prepared system can be used for practical applications (>20 dB). Cotton fabric that was used as a substrate also played a key role in the attenuation process. Its porous nature further increased the multiple internal reflections, thus contributing to the attenuation process.[72,73] Moreover, the high yarn density and weave pattern of the fabric were also responsible for high EMI SE, as discussed earlier in the FE-SEM section where we observed that uniform coating of the dispersion led to formation of a conducting network.

The shielding response measurement of both the samples was repeated after 6 months, and the results are shown in Fig. 8(g)–(i). The SE_T of MX-20 fell from 80 dB to 70 dB (reduction of 12.5%) while the SE_T of MX-10 remained the same at *ca.* 50 dB. These results showed that the samples prepared were suitable for long-term storage and use, making them attractive for practical applications. Excellent designability of fabrics, fabric structure, layers of fabrics, and yarn density are the key features that determine good EMI shielding properties.[74,75] Table S3 shows the calculated value of SE of MX10 and MX20, corresponding to their thickness, along with a literature review. The EMI SE values obtained for the coated fabric are comparable or better than most of the known values in the published work. Finally, a comparison between the shielding parameters of pristine films (under harsh and mild etching condition), heat treated $Ti_3C_2T_x$ thin films and coated fabric, is shown in Fig. 9(c). We conclude that mild etching conditions were suitable for obtaining large flakes, leading to much better and stable $Ti_3C_2T_x$ thin films. Also, temperature had a significant effect on the microstructure and hence, on EMI shielding properties. Moreover, as outlined in Fig. S6, the burning behavior of MXene thin films was studied to assess their flame resistance. The MXene film demonstrates exemplary flame resistance. The findings contribute significantly to the understanding of the correlation of various parameters (etchant type, temperature, flake size, surface chemistry and thickness) in attaining excellent EMI shielding properties, providing opportunities for the development of technologies and devices that mitigate or protect against electromagnetic interference.

Conclusions

In this study, we developed high-performance EMI shielding materials through the rational design of free-standing $Ti_3C_2T_x$ MXene films and functionalized cotton textiles using a scalable vacuum-assisted filtration method. Systematic investigation of etching conditions (LiF + HCl *vs.* HF), thermal treatment, and thickness effects revealed that a heat-treated 5 μm film achieved a remarkable shielding effectiveness of 71 dB, which is 37%

higher than that of untreated films. Moreover, an unprecedented absolute shielding effectiveness (SSE/t) of 72 300 dB cm^2 g^{-1} was recorded, surpassing all comparable MXene-based shields reported to date. The enhanced performance resulted from thermal conversion of surface terminations (–OH to –O), which improved conductivity while simultaneously creating a porous structure that enhanced wave absorption. Comparative analysis showed that LiF + HCl-etched films (71 dB for 5 μm) significantly outperformed HF-etched counterparts (20 dB for 5 μm) due to larger flake sizes, optimized surface chemistry, and superior electrical conductivity. A 13 μm thick film (untreated) exhibited high shielding of 60 dB, demonstrating thickness-dependent performance tunability.

The practical potential was further evidenced by MXene-coated cotton fabric achieving an excellent shielding effectiveness of ~82 dB, representing one of the highest values reported for textile-based shields, while maintaining stable performance after six months of ambient exposure. The exceptional performance originated from synergistic effects, including the fabric's porous meta-structure, large flake sizes, optimized surface dipoles (Ti–O, Ti–F, *etc.*), and high conductivity. These findings provide fundamental insights into the structure–property relationships governing EMI shielding while also establishing a viable manufacturing pathway. The combination of record-breaking performance metrics, environmental stability, and scalable processing positions these MXene-based materials as transformative solutions for next-generation applications in flexible electronics, wearable devices, and aerospace technologies, effectively bridging the gap between scientific innovation and commercial electromagnetic protection needs.

Conflicts of interest

The authors declare that they have no known competing financial interests or personal relationships that could have appeared to influence the work reported in this paper.

Data availability

The data that support the findings of this study are available from the corresponding author, Dr. Shahzad Hussain, upon reasonable request.

Supplementary information is available. See DOI: **https://doi.org/10.1039/d5na00662g**.

References

1 A. Iqbal, F. Shahzad, K. Hantanasirisakul, M.-K. Kim, J. Kwon, J. Hong, H. Kim, D. Kim, Y. Gogotsi and C. M. Koo, Anomalous absorption of electromagnetic waves by 2D transition metal carbonitride Ti_3CNT_x (MXene), *Science*, 2020, **369**, 446–450.

2 S. J. Kazmi, S. U. Rehman, M. Nadeem, U. U. Rehman, S. Hussain and S. Manzoor, Effect of carbon allotropes and thickness variation on the EMI shielding properties of PANI/NFO@ CNTs and PANI/NFO@ RGO ternary composite systems, *Phys. Chem. Chem. Phys.*, 2024, **26**, 10168–10182.

3 S. J. Kazmi, M. Nadeem, M. A. Warsi, S. Manzoor, B. Shabbir and S. Hussain, PVDF/CFO-anchored CNTs ternary composite system with enhanced EMI shielding and EMW absorption properties, *J. Alloys Compd.*, 2022, **903**, 163938.

4 Z. Zeng, F. Jiang, Y. Yue, D. Han, L. Lin, S. Zhao, Y. B. Zhao, Z. Pan, C. Li and G. Nyström, Flexible and ultrathin waterproof cellular membranes based on high-conjunction metal-wrapped polymer nanofibers for electromagnetic interference shielding, *Adv. Mater.*, 2020, **32**, 1908496.

5 S. J. Kazmi, M. Nadeem, A. Younis, S. Loomba, B. Shabbir, S. Manzoor and S. Hussain, PANI/CFO@ CNTs ternary composite system for EMI shielding applications, *J. Magn. Magn. Mater.*, 2022, **563**, 170037.

6 Y. J. Wan, P. L. Zhu, S. H. Yu, R. Sun, C. P. Wong and W. H. Liao, Anticorrosive, ultralight, and flexible carbon-wrapped metallic nanowire hybrid sponges for highly efficient electromagnetic interference shielding, *Small*, 2018, **14**, 1800534.

7 Z. Zeng, H. Jin, M. Chen, W. Li, L. Zhou, X. Xue and Z. Zhang, Microstructure design of lightweight, flexible, and high electromagnetic shielding porous multiwalled carbon nanotube/polymer composites, *Small*, 2017, **13**, 1701388.

8 Z. Zeng, C. Wang, G. Siqueira, D. Han, A. Huch, S. Abdolhosseinzadeh, J. Heier, F. Nüesch, C. Zhang and G. Nyström, Nanocellulose-MXene biomimetic aerogels with orientation-tunable electromagnetic interference shielding performance, *Adv. Sci.*, 2020, **7**, 2000979.

9 I. Hussain, W. U. Arifeen, S. A. Khan, S. Aftab, M. S. Javed, S. Hussain, M. Ahmad, X. Chen, J. Zhao and P. Rosaiah, M_4X_3 MXenes: application in energy storage devices, *Nano-Micro Lett.*, 2024, **16**, 215.

10 A. Younis, E. Idrisov, S. Thaker, F. Hamed, E. H. Sadki, M. Z. Iqbal, T. Mahmood, B. Shabbir and Q. Bao, Advances in MXene-Based Electronics *via* Surface and Structural Redesigning and Beyond, *Adv. Electron. Mater.*, 2025, e00321.

11 D. Nepal, W. J. Kennedy, R. Pachter and R. A. Vaia, Toward architected nanocomposites: MXenes and beyond, *ACS Nano*, 2020, **15**, 21–28.

12 F. Shahzad, M. Alhabeb, C. B. Hatter, B. Anasori, S. Man Hong, C. M. Koo and Y. Gogotsi, Electromagnetic interference shielding with 2D transition metal carbides (MXenes), *Science*, 2016, **353**, 1137–1140.

13 T. Schultz, N. C. Frey, K. Hantanasirisakul, S. Park, S. J. May, V. B. Shenoy, Y. Gogotsi and N. Koch, Surface termination dependent work function and electronic properties of $Ti_3C_2T_x$ MXene, *Chem. Mater.*, 2019, **31**, 6590–6597.

14 X. Sang, Y. Xie, M.-W. Lin, M. Alhabeb, K. L. Van Aken, Y. Gogotsi, P. R. Kent, K. Xiao and R. R. Unocic, Atomic defects in monolayer titanium carbide ($Ti_3C_2T_x$) MXene, *ACS Nano*, 2016, **10**, 9193–9200.

15 K. Maleski, C. E. Ren, M.-Q. Zhao, B. Anasori and Y. Gogotsi, Size-dependent physical and electrochemical properties of two-dimensional MXene flakes, *ACS Appl. Mater. Interfaces*, 2018, **10**, 24491–24498.

16 G. Berdiyorov, Effect of surface functionalization on the electronic transport properties of Ti_3C_2 MXene, *Europhys. Lett.*, 2015, **111**, 67002.
17 L. Dong, H. Kumar, B. Anasori, Y. Gogotsi and V. B. Shenoy, Rational design of two-dimensional metallic and semiconducting spintronic materials based on ordered double-transition-metal MXenes, *J. Phys. Chem. Lett.*, 2017, **8**, 422–428.
18 G. Gao, G. Ding, J. Li, K. Yao, M. Wu and M. Qian, Monolayer MXenes: promising half-metals and spin gapless semiconductors, *Nanoscale*, 2016, **8**, 8986–8994.
19 Q. Tang, Z. Zhou and P. Shen, Are MXenes Promising Anode Materials for Li Ion Batteries? Computational Studies on Electronic Properties and Li Storage Capability of Ti_3C_2 and $Ti_3C_2X_2$ (X = F, OH) Monolayer, *J. Am. Chem. Soc.*, 2012, **134**, 16909–16916.
20 Y. Bai, K. Zhou, N. Srikanth, J. H. Pang, X. He and R. Wang, Dependence of elastic and optical properties on surface terminated groups in two-dimensional MXene monolayers: a first-principles study, *RSC Adv.*, 2016, **6**, 35731–35739.
21 J. L. Hart, K. Hantanasirisakul, A. C. Lang, B. Anasori, D. Pinto, Y. Pivak, J. T. van Omme, S. J. May, Y. Gogotsi and M. L. Taheri, Control of MXenes' electronic properties through termination and intercalation, *Nat. Commun.*, 2019, **10**, 522.
22 M. Anayee, N. Kurra, M. Alhabeb, M. Seredych, M. N. Hedhili, A.-H. Emwas, H. N. Alshareef, B. Anasori and Y. Gogotsi, Role of acid mixtures etching on the surface chemistry and sodium ion storage in $Ti_3C_2T_x$ MXene, *Chem. Commun.*, 2020, **56**, 6090–6093.
23 N. Yousefi, X. Sun, X. Lin, X. Shen, J. Jia, B. Zhang, B. Tang, M. Chan and J. K. Kim, Highly aligned graphene/polymer nanocomposites with excellent dielectric properties for high-performance electromagnetic interference shielding, *Adv. Mater.*, 2014, **26**, 5480–5487.
24 H. Liu, Z. Wang, Y. Yang, S. Wu, C. Wang, C. You and N. Tian, Thermally conductive MWCNTs/Fe_3O_4/$Ti_3C_2T_x$ MXene multi-layer films for broadband electromagnetic interference shielding, *J. Mater. Sci. Technol.*, 2022, **130**, 75–85.
25 M. Q. Zhao, X. Xie, C. E. Ren, T. Makaryan, B. Anasori, G. Wang and Y. Gogotsi, Hollow MXene spheres and 3D macroporous MXene frameworks for Na-ion storage, *Adv. Mater.*, 2017, **29**, 1702410.
26 K. Hu, H. Wang, X. Zhang, H. Huang, T. Qiu, Y. Wang, C. J. Zhang, L. Pan and J. Yang, Ultralight $Ti_3C_2T_x$ MXene foam with superior microwave absorption performance, *Chem. Eng. J.*, 2021, **408**, 127283.
27 Y. Zhang, J. Yu, J. Lu, C. Zhu and D. Qi, Facile construction of 2D MXene ($Ti_3C_2T_x$) based aerogels with effective fire-resistance and electromagnetic interference shielding performance, *J. Alloys Compd.*, 2021, **870**, 159442.
28 L. X. Liu, W. Chen, H. B. Zhang, Q. W. Wang, F. Guan and Z. Z. Yu, Flexible and multifunctional silk textiles with biomimetic leaf-like MXene/silver nanowire nanostructures for electromagnetic interference shielding, humidity monitoring, and self-derived hydrophobicity, *Adv. Funct. Mater.*, 2019, **29**, 1905197.
29 M. A. Ahouei, T. H. Syed, V. Bishop, S. Halacoglu, H. Wang and W. Wei, $Ti_3C_2T_x$ MXene framework materials: Preparation, properties and applications in energy and environment, *Catal. Today*, 2023, **409**, 162–172.
30 L. Geng, P. Zhu, Y. Wei, R. Guo, C. Xiang, C. Cui and Y. Li, A facile approach for coating $Ti_3C_2T_x$ on cotton fabric for electromagnetic wave shielding, *Cellulose*, 2019, **26**, 2833–2847.
31 M. Benchakar, L. Loupias, C. Garnero, T. Bilyk, C. Morais, C. Canaff, N. Guignard, S. Morisset, H. Pazniak and S. Hurand, One MAX phase, different MXenes: A guideline to understand the crucial role of etching conditions on $Ti_3C_2T_x$ surface chemistry, *Appl. Surf. Sci.*, 2020, **530**, 147209.
32 J. Liu, H. B. Zhang, R. Sun, Y. Liu, Z. Liu, A. Zhou and Z. Z. Yu, Hydrophobic, flexible, and lightweight MXene foams for high-performance electromagnetic-interference shielding, *Adv. Mater.*, 2017, **29**, 1702367.
33 W.-T. Cao, F.-F. Chen, Y.-J. Zhu, Y.-G. Zhang, Y.-Y. Jiang, M.-G. Ma and F. Chen, Binary strengthening and toughening of MXene/cellulose nanofiber composite paper with nacre-inspired structure and superior electromagnetic interference shielding properties, *ACS Nano*, 2018, **12**, 4583–4593.
34 Z. Bao, N. Bing, X. Zhu, H. Xie and W. Yu, $Ti_3C_2T_x$ MXene contained nanofluids with high thermal conductivity, super colloidal stability and low viscosity, *Chem. Eng. J.*, 2021, **406**, 126390.
35 O. Mashtalir, *Chemistry of Two-Dimensional Transition Metal Carbides (MXenes)*, Drexel University, 2015.
36 A. Rozmysłowska, T. Wojciechowski, W. Ziemkowska, L. Chlubny, A. Olszyna, S. Poźniak, K. Tomkiewicz and A. Jastrzębska, Colloidal properties and stability of 2D Ti_3C_2 and Ti_2C MXenes in water, *Int. J. Electrochem. Sci.*, 2018, **13**, 10837–10847.
37 Z. Li, L. Wang, D. Sun, Y. Zhang, B. Liu, Q. Hu and A. Zhou, Synthesis and thermal stability of two-dimensional carbide MXene Ti_3C_2, *Mater. Sci. Eng., B*, 2015, **191**, 33–40.
38 N. M. Abbasi, Y. Xiao, L. Peng, Y. Duo, L. Wang, L. Zhang, B. Wang and H. Zhang, Recent advancement for the synthesis of MXene derivatives and their sensing protocol, *Adv. Mater. Technol.*, 2021, **6**, 2001197.
39 Y. Nakatuka, H. Yoshida, K. Fukui and M. Matuzawa, The effect of particle size distribution on effective zeta-potential by use of the sedimentation method, *Adv. Powder Technol.*, 2015, **26**, 650–656.
40 L. Geng, P. Zhu, Y. Wei, R. Guo, C. Xiang, C. Cui and Y. Li, A facile approach for coating $Ti_3C_2T_x$ on cotton fabric for electromagnetic wave shielding, *Cellulose*, 2019, **26**, 2833–2847.
41 M.-K. Xu, J. Liu, H.-B. Zhang, Y. Zhang, X. Wu, Z. Deng and Z.-Z. Yu, Electrically conductive $Ti_3C_2T_x$ MXene/polypropylene nanocomposites with an ultralow percolation threshold for efficient electromagnetic interference shielding, *Ind. Eng. Chem. Res.*, 2021, **60**, 4342–4350.

42 M. Mahmood, A. Rasheed, I. Ayman, T. Rasheed, S. Munir, S. Ajmal, P. O. Agboola, M. F. Warsi and M. Shahid, Synthesis of ultrathin MnO_2 nanowire-intercalated 2D-MXenes for high-performance hybrid supercapacitors, *Energy Fuels*, 2021, **35**, 3469–3478.

43 L. Chen, X. Shi, N. Yu, X. Zhang, X. Du and J. Lin, Measurement and analysis of thermal conductivity of $Ti_3C_2T_x$ MXene films, *Materials*, 2018, **11**, 1701.

44 X. Wang and Y. Zhou, Solid–liquid reaction synthesis of layered machinable Ti_3AlC_2 ceramic, *J. Mater. Chem.*, 2002, **12**, 455–460.

45 K. Maleski, V. N. Mochalin and Y. Gogotsi, Dispersions of two-dimensional titanium carbide MXene in organic solvents, *Chem. Mater.*, 2017, **29**, 1632–1640.

46 R. Sun, H. B. Zhang, J. Liu, X. Xie, R. Yang, Y. Li, S. Hong and Z. Z. Yu, Highly conductive transition metal carbide/carbonitride (MXene)@ polystyrene nanocomposites fabricated by electrostatic assembly for highly efficient electromagnetic interference shielding, *Adv. Funct. Mater.*, 2017, **27**, 1702807.

47 A. Sarycheva and Y. Gogotsi, Raman spectroscopy analysis of the structure and surface chemistry of $Ti_3C_2T_x$ MXene, *Chem. Mater.*, 2020, **32**, 3480–3488.

48 B. Anasori, M. R. Lukatskaya and Y. Gogotsi, 2D metal carbides and nitrides (MXenes) for energy storage, *Nat. Rev. Mater.*, 2017, **2**, 1–17.

49 S. Kumar, H. M. Park, M. Kim, N. Nasir, M. Kumar and Y. Seo, Application dependent stability of $Ti_3C_2T_x$ MXene in PDLC-based smart-windows, *Ceram. Int.*, 2022, **48**, 35092–35099.

50 T. Hu, M. Hu, B. Gao, W. Li and X. Wang, Screening surface structure of MXenes by high-throughput computation and vibrational spectroscopic confirmation, *J. Phys. Chem. C*, 2018, **122**, 18501–18509.

51 R. Rakhi, P. Nayak, C. Xia and H. N. Alshareef, Novel amperometric glucose biosensor based on MXene nanocomposite, *Sci. Rep.*, 2016, **6**, 1–10.

52 A. M. Nair, S. M. Zachariah and S. Thomas, A Mini-Review On MXene Based Textiles For Electromagnetic Interference Shielding Application, Qeios, 2022, preprint, DOI: 10.32388/6wr0r5.

53 P. Sambyal, A. Iqbal, J. Hong, H. Kim, M.-K. Kim, S. M. Hong, M. Han, Y. Gogotsi and C. M. Koo, Ultralight and mechanically robust $Ti_3C_2T_x$ hybrid aerogel reinforced by carbon nanotubes for electromagnetic interference shielding, *ACS Appl. Mater. Interfaces*, 2019, **11**, 38046–38054.

54 S. Hüfner, *Photoelectron Spectroscopy: Principles and Applications*, Springer Science & Business Media, 2013.

55 Y. Zhang, K. Ruan, X. Shi, H. Qiu, Y. Pan, Y. Yan and J. Gu, $Ti_3C_2T_x$/rGO porous composite films with superior electromagnetic interference shielding performances, *Carbon*, 2021, **175**, 271–280.

56 T. Zhang, L. Pan, H. Tang, F. Du, Y. Guo, T. Qiu and J. Yang, Synthesis of two-dimensional $Ti_3C_2T_x$ MXene using HCl+ LiF etchant: enhanced exfoliation and delamination, *J. Alloys Compd.*, 2017, **695**, 818–826.

57 P. Liu, Z. Yao, V. M. H. Ng, J. Zhou, L. B. Kong and K. Yue, Facile synthesis of ultrasmall Fe_3O_4 nanoparticles on MXenes for high microwave absorption performance, *Compos. Appl. Sci. Manuf.*, 2018, **115**, 371–382.

58 X. Zhang, H. Wang, R. Hu, C. Huang, W. Zhong, L. Pan, Y. Feng, T. Qiu, C. J. Zhang and J. Yang, Novel solvothermal preparation and enhanced microwave absorption properties of $Ti_3C_2T_x$ MXene modified by *in situ* coated Fe_3O_4 nanoparticles, *Appl. Surf. Sci.*, 2019, **484**, 383–391.

59 J. Zhang, N. Kong, S. Uzun, A. Levitt, S. Seyedin, P. A. Lynch, S. Qin, M. Han, W. Yang and J. Liu, Scalable manufacturing of free-standing, strong $Ti_3C_2T_x$ MXene films with outstanding conductivity, *Adv. Mater.*, 2020, **32**, 2001093.

60 H. Huang, H. Su, H. Zhang, L. Xu, X. Chu, C. Hu, H. Liu, N. Chen, F. Liu and W. Deng, Extraordinary areal and volumetric performance of flexible solid-state micro-supercapacitors based on highly conductive freestanding $Ti_3C_2T_x$ Films, *Adv. Electron. Mater.*, 2018, **4**, 1800179.

61 M. Han, X. Yin, H. Wu, Z. Hou, C. Song, X. Li, L. Zhang and L. Cheng, Ti_3C_2 MXenes with modified surface for high-performance electromagnetic absorption and shielding in the X-band, *ACS Appl. Mater. Interfaces*, 2016, **8**, 21011–21019.

62 H. Shao, in *2D $Ti_3C_2T_x$ MXenes for Electrochemical Energy Storage*, Université Paul Sabatier-Toulouse III, 2020.

63 A. Iqbal, P. Sambyal and C. M. Koo, 2D MXenes for electromagnetic shielding: a review, *Adv. Funct. Mater.*, 2020, **30**, 2000883.

64 S.-Y. Kim, H.-E. Gang, G.-T. Park, H.-B. Jeon and Y. G. Jeong, Electromagnetic Interference Shielding and Electrothermal Performance of MXene-Coated Cellulose Hybrid Papers and Fabrics Manufactured by a Facile Scalable Dip-Dry Coating Process, *Adv. Eng. Mater.*, 2021, **23**, 2100548.

65 M. A. Hope, A. C. Forse, K. J. Griffith, M. R. Lukatskaya, M. Ghidiu, Y. Gogotsi and C. P. Grey, NMR reveals the surface functionalisation of Ti_3C_2 MXene, *Phys. Chem. Chem. Phys.*, 2016, **18**, 5099–5102.

66 G. Hu, Z. Cen, Y. Xiong and K. Liang, Progress of high performance $Ti_3C_2T_x$ MXene nanocomposite films for electromagnetic interference shielding, *Nanoscale*, 2023, **15**, 5579–5597.

67 X.-A. Ye, S.-Y. Zhang, D.-Q. Zhao, L. Ding, K. Fang, X. Zhou and G.-G. Wang, Super-flexible and highly conductive H-$Ti_3C_2T_x$ MXene composite films with 3D macro-assemblies for electromagnetic interference shielding, *Compos. Appl. Sci. Manuf.*, 2024, **176**, 107866.

68 C. Qiao, H. Wu, X. Xu, Z. Guan and W. Ou-Yang, Electrical conductivity enhancement and electronic applications of 2D $Ti_3C_2T_x$ MXene materials, *Adv. Mater. Interfaces*, 2021, **8**, 2100903.

69 Y. Yang, Z. Cao, L. Shi, R. Wang and J. Sun, Enhancing the conductivity, stability and flexibility of $Ti_3C_2T_x$ MXenes by regulating etching conditions, *Appl. Surf. Sci.*, 2020, **533**, 147475.

70 D. Magne, V. Mauchamp, S. Célérier, P. Chartier and T. Cabioc'h, Site-projected electronic structure of two-

dimensional Ti_3C_2 MXene: the role of the surface functionalization groups, *Phys. Chem. Chem. Phys.*, 2016, **18**, 30946–30953.

71 M. Hu, T. Hu, Z. Li, Y. Yang, R. Cheng, J. Yang, C. Cui and X. Wang, Surface functional groups and interlayer water determine the electrochemical capacitance of $Ti_3C_2T_x$ MXene, *ACS Nano*, 2018, **12**, 3578–3586.

72 Y. Cheng, X. Li, Y. Qin, Y. Fang, G. Liu, Z. Wang, J. Matz, P. Dong, J. Shen and M. Ye, Hierarchically porous polyimide/$Ti_3C_2T_x$ film with stable electromagnetic interference shielding after resisting harsh conditions, *Sci. Adv.*, 2021, **7**, eabj1663.

73 A. Iqbal, J. Kwon, M.-K. Kim and C. Koo, MXenes for electromagnetic interference shielding: Experimental and theoretical perspectives, *Mater. Today Adv.*, 2021, **9**, 100124.

74 S. Uzun, M. Han, C. J. Strobel, K. Hantanasirisakul, A. Goad, G. Dion and Y. Gogotsi, Highly conductive and scalable $Ti_3C_2T_x$-coated fabrics for efficient electromagnetic interference shielding, *Carbon*, 2021, **174**, 382–389.

75 W. Cheng, Y. Zhang, W. Tian, J. Liu, J. Lu, B. Wang, W. Xing and Y. Hu, Highly efficient MXene-coated flame retardant cotton fabric for electromagnetic interference shielding, *Ind. Eng. Chem. Res.*, 2020, **59**, 14025–14036.